ACS APPLIED MATERIALS & INTERFACES
Research Article
www.acsami.org

Facile Fabrication of Hierarchically Porous $CuFe_2O_4$ Nanospheres with Enhanced Capacitance Property

Maiyong Zhu,[†,‡] Dehai Meng,[†] Chengjiao Wang,[†] and Guowang Diao*,[†]

[†]College of Chemistry and Chemical Engineering, Yangzhou University, Yangzhou, Jiangsu Province, 225002, People's Republic of China

[‡]School of Materials Science & Engineering, Jiangsu University, Zhenjiang, Jiangsu Province, 212013, People's Republic of China

Supporting Information

ABSTRACT: In this work, $CuFe_2O_4$ nanospheres with hierarchically porous structure have been synthesized via a facile solvothermal procedure. The superstructures consist of the textured aggregations of nanocrystals with high specific surface area, pore volume, and uniform pore size distribution.- To figure out the formation mechanism, we discussed in detail the effects of a series of experimental parameters, including the concentrations of the precipitation agent, stabilizer agent, and reaction temperature and time on the size and morphology of the resulting products. Furthermore, the electrochemical properties of $CuFe_2O_4$ nanospheres were evaluated by cyclic voltammetry and galvanostatic charge-dischrge studies. The results demonstrate that the as-prepared $CuFe_2O_4$ nanospheres are excellent electrode material in supercapacitor with high specific capacitance and good retention. The hierarchically $CuFe_2O_4$ nanospheres show the highest capacitance of 334F/g, and 88% of which can still be maintained after 600 charge−discharge cycles.

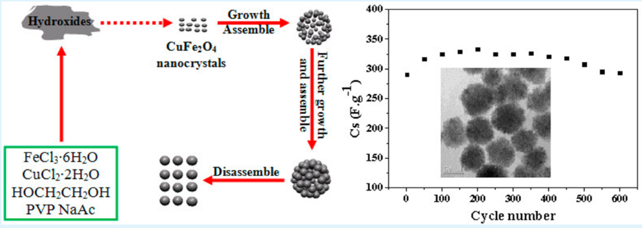

KEYWORDS: *$CuFe_2O_4$, solvothermal procedure, hierarchically porous, supercapacitor*

1. INTRODUCTION

Supercapacitors, also named electrochemical capacitors or ultracapacitors, which are widely used in energy backups, electric vehicles, and portable devices, have attracted increasing interest. Compared to lithium-ion batteries as well as conventional dielectric capacitors, supercapacitors provide higher power and energy density.[1−5] Also, Supercapacitors have the advantages of short charging times and longer cycle as well as self-life.[6,7] The crucial task for constructing a supercapacitor is exploring the electrode material meeting the desired requirements. Among the array of electrode materials for supercapacitor applications, RuO_2 has been recognized as the most promising one due to its excellent capacitive response. However, the high cost as well as environmentally poisonous nature has limited its application in practice.[8−12]

To develop economical electrode materials with not only a high capacity of charge storage but also energy density, attentions have been paid to cheap metal oxides with comparable characteristics during the past years. For example, oxides of Ni,[13−15] Co,[16−20] Fe,[21,22] Mo,[23] V,[24] Mn,[25−30] and so forth have been explored as supercapacitor electrode materials as substitutes of RuO_2.[31,32] Although significant progress has been made during the past years in reducing the cost of electrode materials for supercapacitors, next-generation supercapacitors with longer cycling lifetime and higher energy density is still desirable. Transition metal oxides with cubic spinel structure have been proved favorable for supercapacitors.[33−39] In particular, $CuFe_2O_4$ with an inverse spinel structure has been widely regarded as one of the promising anode materials for supercapacitors owing to its convenient obtaining and environmental benignity. Very recently, the capacitance characteristic of $CuFe_2O_4$ hollow fibers obtained by simple electrospinning and direct annealing by Zhao and his co-workers, have been demonstrated to be pseudocapacitive capacitance.[40]

In this context, here we first reported the synthesis of hierarchically porous $CuFe_2O_4$ nanospheres by a solvothermal process and their characterization by diverse techniques. And then the formation mechanism of the product was investigated by changing various experiment parameters. Finally, the as-prepared hierarchically porous $CuFe_2O_4$ nanospheres were tested as electrodes for supercapacitors. The spaces between $CuFe_2O_4$ nanocrystals arranged into hierarchically porous structure allow easy diffusion of electrolyte into the inner region of the electrode, which may efficiently accelerate electrode reactions. So the internal resistance is reduced and the capacitance performance would be improved to some extent.

2. EXPERIMENTAL SECTION

2.1. Materials Preparation. All chemicals were of analytic grade and used as received without further purification. Hierarchically porous

Received: February 27, 2013
Accepted: June 10, 2013
Published: June 10, 2013

dx.doi.org/10.1021/am4007353 | *ACS Appl. Mater. Interfaces* 2013, 5, 6030−6037

$CuFe_2O_4$ nanospheres were successfully fabricated through the hydrothermal method. Important parameters, including the concentration of anhydrous sodium acetate(NaAc), the type as well as the concentration of stabilization agent, the reaction time and temperature, were altered in a series of parallel experiments to investigate the formation mechanism. In a typical preparation, the procedure is as follows: 2 mmol $CuCl_2 \cdot 2H_2O$, 4 mmol $FeCl_3 \cdot 6H_2O$, 6 mmol NaAc, and 0.5 g of polyvinylpyrrolidone (PVP) were dissolved into 30 mL of ethylene glycol by stirring. The mixture was sealed in a Teflon-lined autoclave and maintained at 160 °C for 24 h. The solid precipitates were collected using a magnet after the mixture was cooled down to room temperature. To remove the residual of metal ions and organic moiety, we washed the products several times using deionized water and ethanol. At last, the products were dried under vacuum at 70 °C for 12 h.

2.2. Materials Characterization. Transmission electron microscopy (TEM) and high-resolution TEM (HRTEM) were measured on a Philips Tecnai G2 F20 transmission electron microscope. The X-ray powder diffraction (XRD) pattern was performed on a D8 Advance (Super speed) XRD diffractometer (Bruker). The X-ray photoelectron spectroscopy (XPS) experiments were tested on a Thermo Escalab 250 system using Al Kα radiation ($h\nu$ = 1486.6 eV). The pressure of test chamber was maintained below 2×10^{-9} Torr during spectral acquisition. The Brunauer−Emmett−Teller (BET) specific surface areas of typical products were performed at 77 K in a Micromeritics ASAP 2010 system.

2.3. Electrochemical Measurements. Before electrochemical testing, an electrode was fabricated by mixing 70 wt % of $CuFe_2O_4$ with 15 wt % acetylene black, 15 wt % polyvinylidene difluoride (PVDF) in N-methyl-2-pyrrolidinone (NMP). And then, the slurry was coated on a pretreated battery-grade polished Ni foil (area of coating: 1 cm^2, the thickness of Ni Foil is 0.2 mm) for electrical conductivity and vacuum-dried at 60 °C for 8 h.

A three-electrode cell was fabricated employing a saturated calomel electrode (SCE) as the reference electrode, the as-prepared electrode as working electrode and platinum wire electrode as counter electrode, respectively. All electrochemical tests were performed on an electrochemical workstation (CHI 660C, Chenhua, Shanghai), and the electrolyte used was 1 M aqueous KOH solution.

3. RESULTS AND DISCUSSION

3.1. Characterization of $CuFe_2O_4$ Nanospheres.

The hierarchically porous $CuFe_2O_4$ nanospheres was prepared with the reaction of $CuCl_2 \cdot H_2O$, $FeCl_3 \cdot H_2O$, and NaAc in presence of PVP under a hydrothermal condition. The morphology as well as the size of the typical sample was characterized by transmission electron microscopy (TEM). From the TEM images (Figure 1A, B), it can be clearly observed that the samples exhibit a hierarchical profile of 3-dimensional sphere-like micro/nanostructure. Each sample with different structure is assembled with primary small particles. The surface of the nanospheres is very rough. The size of these nanostructures is not very uniform with the average diameter of ca. 60 nm. High-resolution transmission electron microscopy (HRTEM) was used to further understand the dimensionality of the nanosphere morphologies. Figure 1C displays the lattice resolved HRTEM image of $CuFe_2O_4$ nanocrystal. It was clearly observed that inter planar spacing is measured to be 0.256 nm, which is corresponded to the (311) crystal planes of $CuFe_2O_4$ with cubic spinel structure.[41] In addition, selected area electron diffraction (SAED) pattern of $CuFe_2O_4$ nanospheres is also performed to obtain more structure information of the prepared $CuFe_2O_4$ nanospheres. From Figure 1D, the diffraction rings can be seen, which should be attributed to the cubic spinel $CuFe_2O_4$ crystal structure.

The crystal structure of the product was examined using X-ray diffraction pattern (XRD). As can be seen from Figure 2, the position and relative intensity of diffraction peaks are in accordance with those of $CuFe_2O_4$ (JCPDS 25−0283) and no peaks of copper oxides (CuO or CuO_2) were observed. Here it should be pointed out that the obvious amorphous phase in the XRD pattern belongs to hydroxides. These peaks at 2θ = 30.1, 35.4, 43.1, 50.3, 53.4, 57.0, 62.5, and 74.0° are ascribed to (220), (311), (400), (107), (422), (511), (440), and (533) reflections of $CuFe_2O_4$ with cubic spinel structure. It is noted that the $CuFe_2O_4$ (311) peak has the highest intensity implying the oriented growth of the sample alongside the (311) direction. Moreover, the relatively high peak intensities imply that the products are highly crystalline.

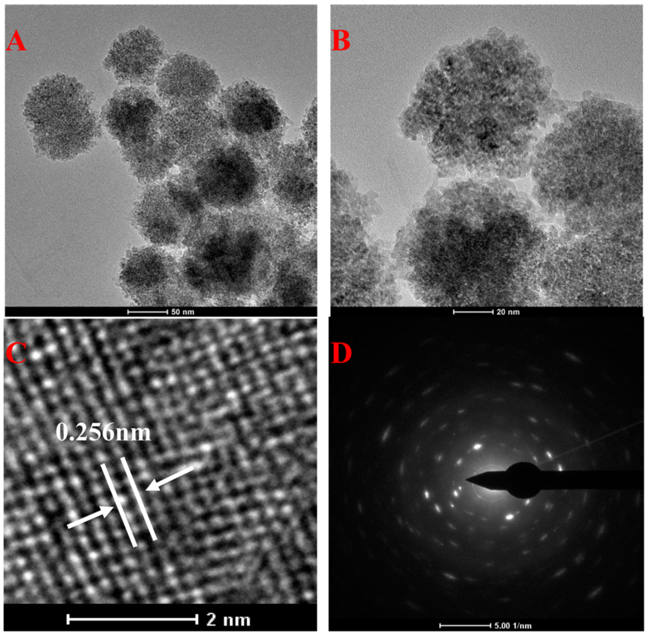

Figure 1. (A, B) TEM images of the as-prepared $CuFe_2O_4$ nanospheres with different magnifications. (C) Lattice-resolved HRTEM image of a part of $CuFe_2O_4$ nanospheres. (D) Selected area electron diffraction pattern of $CuFe_2O_4$ nanospheres.

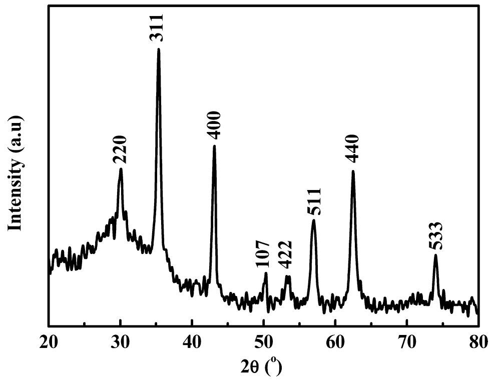

Figure 2. XRD pattern of the as-prepared $CuFe_2O_4$.

To further verify the composition of the prepared products, we applied XPS analysis to investigate both the concentration and binding energy of surface atoms present in the as-synthesized $CuFe_2O_4$ nanospheres. In the survey spectrum (Figure 3A), the elements Cu, Fe, and O can be observed clearly. The appearance of C1s and N1s peaks can be ascribed to the adsorbed or bonded organic species. The binding energy values of Fe2p and Cu2p for the sample were found to be 710.5

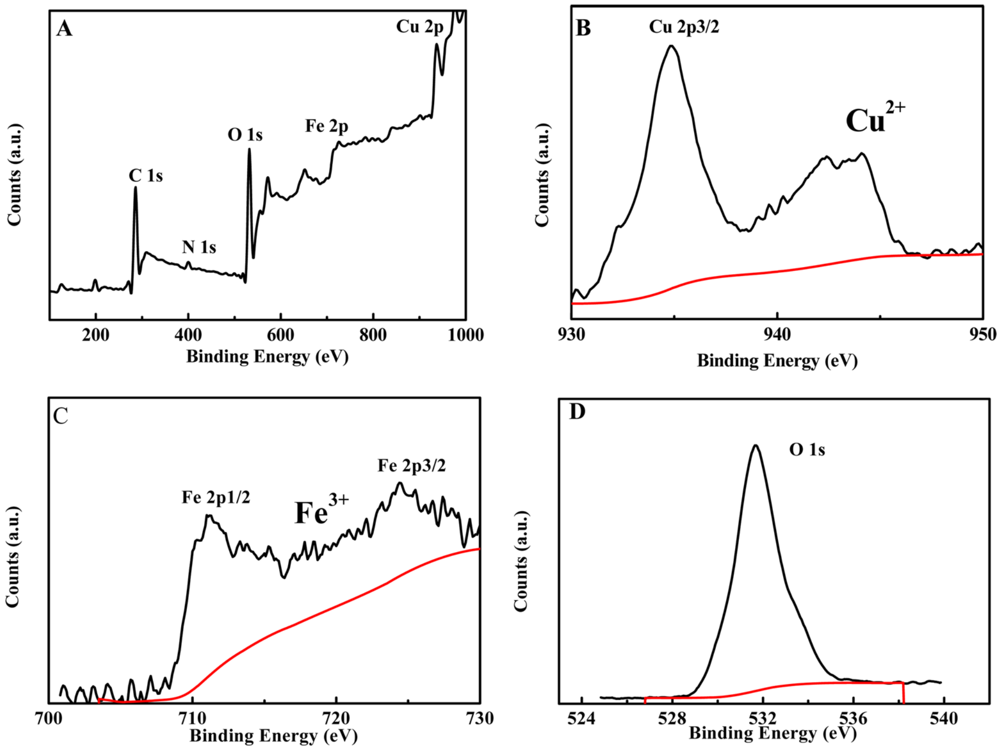

Figure 3. (A) Wide and (B−D) deconvoluted XPS spectra of the as-prepared hierarchically porous $CuFe_2O_4$ nanospheres.

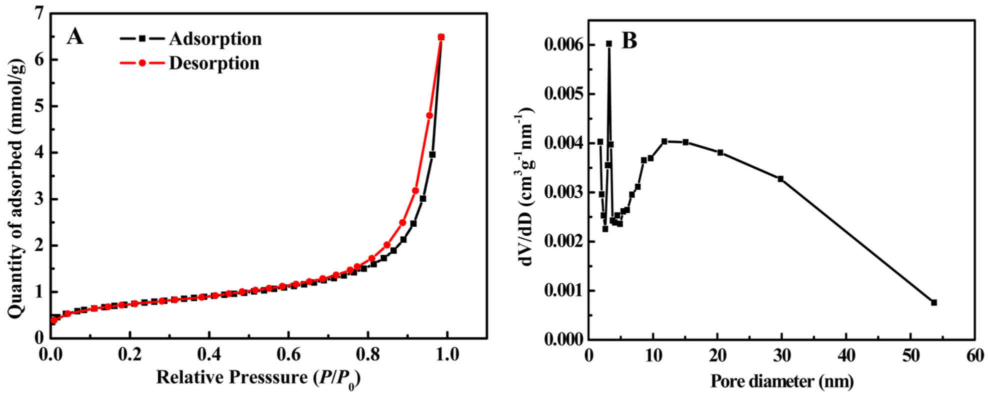

Figure 4. (A) Nitrogen adsorption−desorption isotherms and (B) corresponding pore size distribution curves of the $CuFe_2O_4$ nanospheres.

and 936.7 eV, respectively. The obtained results obviously implied that both iron ions and copper ions are present in $CuFe_2O_4$ powders. One can see from Figure 3B that the high-resolution XPS spectrum of Cu 2p shows that Cu is in the +2 oxidation state in the product. The binding energy of Cu2p3/2 and Cu2p1/2 are 934.8 and 944.1 eV, which is in conformity with the results reported elsewhere.[42] As for the Fe 2p core level peak, one can see from Figure 3 C that the iron exists in the Fe(III) oxidation state, without any impurity of the Fe(II) oxidation state. In addition, the O 1s core level peak, centered at 529.4 eV displayed in Figure 3D, belongs to the O^{2-} contribution.

To evaluate the specific surface areas and porosity of the hierarchically porous $CuFe_2O_4$ nanospheres, we measured N_2 adsorption−desorption isotherms. As shown in Figure 4A, the isotherm of the $CuFe_2O_4$ nanosphere exhibits a typical IUPAC type IV pattern, suggesting the presence of mesopores. The BET specific surface area of the product is ca. 57.7 m^2 g^{-1}, which is nearly twice as large as that reported by Fu et al.[41] The pore size distributions are calculated from the desorption branch of the nitrogen isotherm using the BJH method. The bimodal mesopore size distribution is further confirmed by the corresponding pore size distributions (Figure 4B). The irregular pore size distribution may be resulted from two factors. First, the primary nanocrystals in each nanosphere were aggregated in a random manner. Second, the sizes of the primary nanocrystals were not completely uniform.

3.2. Formation Mechanism of $CuFe_2O_4$ Nanospheres.

During the preparation of Fe_3O_4 and Fe_2O_3 nanostructures from the hydrothermal method we learned that the experimental conditions have significant influence on the quality of the obtained nanomaterial. For that reason, some potential influencing factors toward the synthesis route were investigated, which may helpful to understand the formation mechanism of the hierarchically porous $CuFe_2O_4$ nanospheres.

3.2.1. Effect of NaAc Concentration. To investigate the effect of the amount of NaAc on the morphology of $CuFe_2O_4$ nanostructures, a number of experiments were carried out by changing the amount of NaAc, whereas other parameters were fixed. When 6 mmol NaAc is in the initial solution, the as-synthesized sample exhibits uniform nanospheres with the average diameter of 60 nm (see Figure S1A in the Supporting Information). By contrast, when more NaAc (9 mmol) was added to the initial solution, solid spheres can be obtained (see Figure S1B in the Supporting Information). Moreover, the size is much larger than that prepared while using 6 mmol NaAc. If the NaAc amount was further increased to 12 mmol, the size of the solid spheres increases from ca. 200 nm to ca. 300 nm, as one can see in Figure S1C in the Supporting Information.

The effect of NaAc amount on the morphology of the product can be explained as follows. It has been accepted for metal oxides that the particle morphology is strongly dependent on the pH of the solution system. Typically, the formation of $CuFe_2O_4$ nanospheres in hydrothermal system includes three processes: nucleation of nanocrystals, growth of nanocrystals and assemble. These three processes may occur simultaneously. If the amount of NaAc is low, the nucleation step for the formtion of $CuFe_2O_4$ may be prevented. Under such circumstances, the growth step and the followed assemble process are preferable, leading to uniform-structured nanospheres, while the case might be different for high amount of NaAc. For one thing, once the superfluous NaAc was added, it could act as a mineralizer and increase the chemical potential of the solution, which may result in a dissolution−recrystallization process of $CuFe_2O_4$ into the stable phase with a bigger size. For another thing, high OH^- concentration, generated by high concentration of NaAc, would lead to an enhanced ionolysis rate of the metal ion which typically leads to agglomerated, spherical particles.[43] Thus, products with larger sizes will be obtained as shown in Figure S1 B, C in the Supporting Information.

3.2.2. Effect of the Stabilization Agent. It has been proved that surfactants, which are amphiphilic molecules generally consisting of at least one hydrophilic headgroup and one hydrophobic chain, play important roles in controlling the size as well as the morphology of micro/nanomaterials. First of all, we prepared three products using different surfactants as the stabilization agent. Figure S2 in the Supporting Information shows the TEM images of $CuFe_2O_4$ obtained using different surfactants as morphology-directing reagents. In the investigated surfactant amount (0.5g) sodium dodecyl sulfate (SDS) shows little positive influence on controlling the morphology of $CuFe_2O_4$. As shown in Figure S2A in the Supporting Information, most part of the product shows the agglomerated structures without regular assemble collections. Contrarily, PVP greatly controlled the crystal morphology of $CuFe_2O_4$ as the assembled nanospheres with the average diameter of ca. 60 nm, and the size distribution is narrow (see Figure S2B in the Supporting Information). As for hexadecyl trimethyl ammonium bromide (CTAB), one typical cationic surfactant, the morphology of the obtained $CuFe_2O_4$ is flower-shaped structures composed of many primary nanocrystals (see Figure S2C in the Supporting Information). Also, the average diameter is over 100 nm, which is much larger than that of sample in Figure S2B in the Supporting Information.

Besides the effect of the types of surfactant, we also checked the effect of the amount of PVP on the morphology and structure of the $CuFe_2O_4$ nanospheres. Figure S3 in the Supporting Information shows the samples synthesized with different quantities of PVP at 160 °C for 24 h. When the reaction was carried out without PVP, not nanospheres but the agglomerated nanoparticles were observed as the sole product in Figure S3A in the Supporting Information. This can be explained as follows. Under basic conditions, OH^- ions were predominately adsorbed onto the surface of $CuFe_2O_4$, leading to the existence of plenty of surface hydroxyls for the obtained $CuFe_2O_4$ nanocrystals. When a relatively low amount of PVP (0.25 g) was introduced into the synthesis system, some spherelike structures could be obtained accompanying solid spheres and the sizes are not uniform. The average size of these spheres is larger than 200 nm (see Figure S3B in the Supporting Information). With a further increase in the quantity of PVP to 0.5 g, the solid structures are disappeared, indicating the template effect of PVP for growing assembled porous structures is dominant in this condition. Also, the size distribution is most satisfied (Figure 1A, B). In contrast, the dispersity of products will deteriorate when PVP is excessive (1.0 g), as can be seen from Figure S3C in the Supporting Information.

The role of PVP amount on the quality of the spheres can be explained depending on the capping effect. When a small amount/no PVP were in applied, the capping effect would be not sufficient for the effective coverage or passivation of $CuFe_2O_4$ crystals, thus only aggregation of the particles arrayed in freedom would be obtained. Only suitable amount of PVP, adsorbed on the crystals, may prevent the aggregation of the particles for either stero-barrier interaction or electrostatic repulsive. Although the capping effect will be enhanced with increasing PVP concentration, a critical point will seem to be reached beyond which two behaviors may occur. On one hand, micelles or reverse micelles, forming at high PVP concentration, cannot induce the crystal as desired. On the other hand, the excessive free PVP (not adsorbed on the crystals) would affect the growth and assembly process of $CuFe_2O_4$. Under this condition, larger and smaller structures grow up simultaneously. This can be contributed to the inhomogeneous templates formed by excessive PVP in solution at the initial growth stage.

3.2.3. Effect of Reaction Temperature. For exploring how reaction temperature affects the formation of $CuFe_2O_4$ nanospheres, a series of contrasting experiments were conducted. Figure S4 in the Supporting Information shows the TEM images of $CuFe_2O_4$ prepared at 140, 180, and 200 °C, respectively. As shown in Figure S4A in the Supporting Information, no $CuFe_2O_4$ nanospheres but the agglomerated nanoparticles as the sole product were observed when the reaction was carried out bellow 140 °C. The case is different when the reaction temperature was raised to 160 °C. Regular $CuFe_2O_4$ nanospheres consisting of many primary nanocrystals can be obtained as shown in Figure 1 A, B. Meanwhile, the average diameter of these nanospheres was ca. 60 nm. Unfortunately, the products prepared at higher temperatures, the morphologies of $CuFe_2O_4$ changed significantly. From Figure S4B, C in the Supporting Information, we can see that the $CuFe_2O_4$ products obtained at 180 and 200 °C are irregular particles (spherelike particles and polygonlike grains coexist) with sizes of less than 50 nm. From Figure S4D in the Supporting Information, the XRD patterns reveal that all products obtained at 140, 180, and 200 °C were $CuFe_2O_4$.

The effect of temperature in this system can be attributed to interaction between the colloidal $CuFe_2O_4$ nanocrystal and PVP. When the temperature is very low (140 °C or lower), there will be a large number of surface hydroxyls for the obtained $CuFe_2O_4$ nanocrystals since OH^- ions were predominately adsorbed onto the surface of $CuFe_2O_4$. The

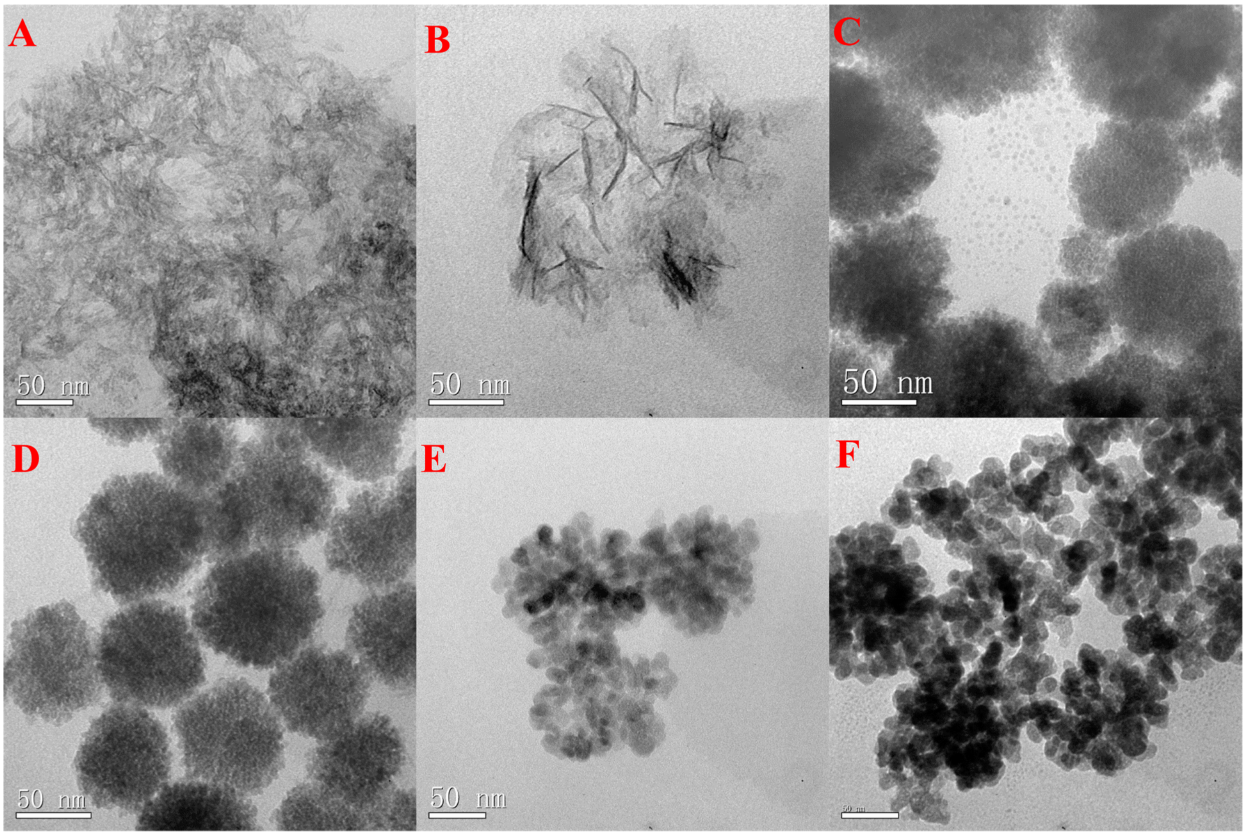

Figure 5. TEM images of the products collected at different reaction times: (A) 12, (B) 18, (C) 21, (D) 24, (E) 36, and (F) 48 h. Other conditions: 2 mmol of $CuCl_2·2H_2O$, 4 mmol of $FeCl_3·6H_2O$, 6 mmol of NaAc, 0.5 g of PVP, 30 mL of ethylene glycol, 160 °C.

attraction from the elimination of surface hydroxyls on the adjacent particles, via condensation reaction dehydration between two surfaces under basic conditions, will result in the aggregation of $CuFe_2O_4$ nanocrystals. As for high temperatures (180 and 200 °C), the PVP molecules can not be effectively adsorbed on the surface of $CuFe_2O_4$ nanocrystals, preventing the assemble process. In our experiments, the most suitable temperature for obtaining assemble-structured $CuFe_2O_4$ nanospheres is 160 °C.

3.2.4. Effect of Reaction Time. The time-dependent experiments were carried out to investigate the formation mechanism of the hierarchically porous $CuFe_2O_4$ nanospheres. The experimental results are depicted in Figure 5. As shown in Figure 5A, at earlier stage (12 h), the sample was composed of structures with no uniform morphology. The sample collected 18 h later (Figure 5B) showed plated shape. With the reaction processed, nanosphere structure consisting of many primary crystals appeared (Figure 5C, 21 h), though the size as well as the interspace between these primary crystals was not very clear. After 24 h (Figure 5D), the amount of nanospheres increased. At the same time, the size of the 3D nanostructure grew gradually and the morphology became spherical. Interestingly, when the reaction time was prolonged to 36 or 48 h, the assembled nanospheres disassembled. Only agglomerated nanoparticles sized in about 10 nm were obtained, as shown in Figure 5E, F.

Besides morphology investigation, the crystalline evolution of the time-dependent product was also studied in our system. Figure 6 shows the XRD patterns of the products collected at different reaction times. When the reaction time is 12 h (curve A), only several broaden peaks are observed, indicating that precursor have begun to convert into amorphous $CuFe_2O_4$ at the initial stage. It is the hydroxides of copper and iron. In curve B (reaction time of 18h), one can see that the broaden peaks disappeared and the peak according to (311) crystal planes of $CuFe_2O_4$ with cubic spinel structure appeared. This phenomenon suggests that the $CuFe_2O_4$ in our system will grow oriented with (311) crystal plane. Prolonging reaction time to 21h, new diffraction peaks associated with planes of (220), (400), (107), (422), (511), (440), and (533) appear (curve C). When the reaction time is increased to 24 h, the intensities of the diffraction peaks (curve D) increase significantly compared with those in curve C, implying enhanced crystallinity. Furthermore, the diffraction peaks of the $CuFe_2O_4$ phase are markedly degenerative compared with the sample prepared with a reaction time of 21 h, which indicates a phase transition

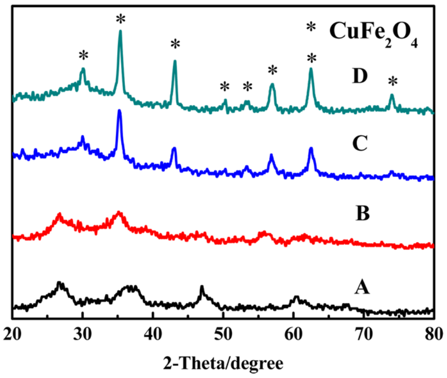

Figure 6. XRD patterns of the products collected at different reaction time. (A) 12, (B) 18, (C) 21, (D) 24 h.

and dissolution−recrystallization process. In addition, no diffraction peak attributed to Fe_2O_3 or CuO is detected, which indicates that the product is pure $CuFe_2O_4$.

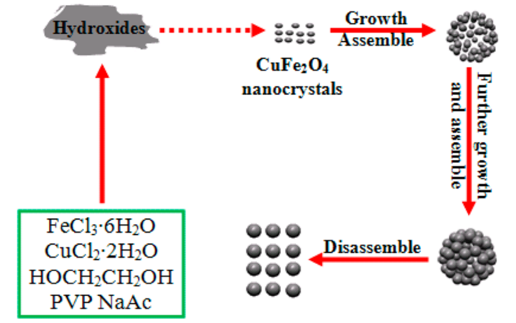

Figure 7. Schematic illustration for the plausible formation mechanism of the hierarchically porous $CuFe_2O_4$ nanospheres.

On the basis of the above discussions, the possible formation mechanism of hierarchically porous $CuFe_2O_4$ nanospheres in our system could be clearly illustrated in Figure 7. At the initial period of the hydrothermal synthesis, Cu^{2+} and Fe^{3+} were precipitated under the basic condition to amorphous hydroxides which show plate-shaped structure. The plated amorphous hydroxides are easy to dehydrate, forming $CuFe_2O_4$ nanocrystals. Through interacting with PVP, the formed $CuFe_2O_4$ nanocrystals then assembled into hierarchically porous $CuFe_2O_4$ nanospheres. Unfortunately, these assembled hierarchically porous structures may not well thermal stability. They can disassemble forming agglomerated $CuFe_2O_4$ nanoparticles.

As for the driving force for oriented aggregation of nanocrystals, it can be generally attributed to two factors. On one hand, to reduce the high surface energy the nanocrystals are tend to aggregate through both the attachment among the primary nanoparticles as well as the rotation of these primary nanoparticles.[44,45] On the other hand, the $CuFe_2O_4$ nanoparticles stabilized with PVP can form an almost perfect oriented structure within aggregated spheres. And it is believed that PVP molecules, which attached on the surface of the $CuFe_2O_4$ nanoparticles in the nonaqueous system, play an important role in forming such an oriented aggregation by facilitating the rotation of the $CuFe_2O_4$ nanoparticles.

3.3. Electrochemical Tests.

As the $CuFe_2O_4$ nanospheres are composed of numerous primary nanocrystals with very small size, and possess high surface area as well as mesoporosity, the transportation of electrolytes through their mesopores is possibly more feasible for efficient redox reactions during Faradic charge storage process. Hence, the electrochemical performance of the as-prepared hierarchically porous $CuFe_2O_4$ nanospheres was studied using a three-electrode system. Several electrochemical techniques, including cyclic voltammetry (CV), galvanostatic charge−discharge, and constant current discharge have been employed in this study.

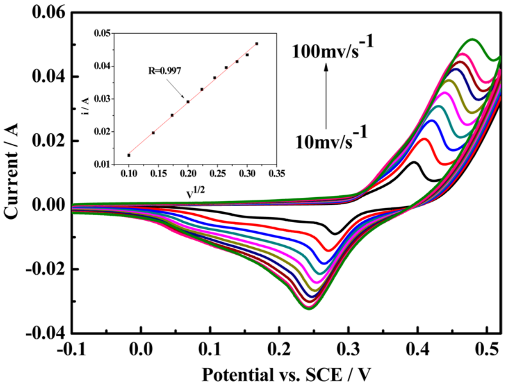

Figure 8. CV curves of the electrodes made from the hierarchically porous $CuFe_2O_4$ nanospheres for supercapacitors application in the range of −0.1 to 0.5 V at various scan rates.

The CV measurements have been performed at various sweep rates in a fixed potential range of −0.1−0.52 V (versus SCE) to evaluate the rate dependent supercapacitive performance of the hierarchically porous $CuFe_2O_4$ nanospheres. As shown in Figure 8, a pair of cathodic and anodic peaks in the CV curves can be clearly found, indicating the fast redox reaction of $CuFe_2O_4$ in alkaline solution. The redox process can be described as follows

$$CuFe_2O_4 + H_2O + 2e^- \rightleftharpoons CuO + 2FeO + 2OH^-$$

In addition, the peak current value show linear relationship to the square root of the scanning rate (inset), suggesting that the electrochemical reaction occurring on the electrode surface is a diffusion-controlled process.

Furthermore, to investigate the cyclic performance and stability of an electrode material, extensive charge−discharge cyclic measurements were performed at different current densities. Figure 9A shows the rate dependent discharge profile for the hierarchically porous $CuFe_2O_4$ nanospheres at gravimetric current densities of 1.0, 0.9, 0.8, 0.7, 0.6, 0.5, 0.4, 0.3, 0.2, and 0.1 A g^{-1}. The specific capacitance of the electrode could be calculated according to the following equation[46]

$$C = \frac{I}{[(dV/dt)w]}$$

where I (mA) and dV/dt (mV s^{-1}), respectively, denote the applied galvanostatic current and the slope of chronopentionmetric curve; w (g) represents the mass of electroactive material. The relation between the specific capacitance and the current density is plotted as in Figure 9B. It is noted that the largest capacitance value could be reached up to 289.5 F g^{-1} when the current density is 0.6 A g^{-1}. The results suggest that the material has good rate capacitance. The specific capacitance value of $CuFe_2O_4$ nanospheres reported here is higher than that of some reported literatures. For example, Zhao et al. reported the fabrication of $CuFe_2O_4$ hollow fibers by electrospinning and direct annealing, showing specific capacitance of 28 F g^{-1} at 0.5 A g^{-1}.[40] Similarly, Ham et al. reported the specific capacitance of 5.7 F g^{-1} at 0.3 μA cm^{-2} for $CuFe_2O_4$ thin films synthesized by spray-pyrolysis method.[47]

It is well-known that the surface adsorption of electrolyte anions (OH^-) on metal oxide electrode is determinable for charge storage behavior. When the charge current density is very low (less than 0.6 A g^{-1}), the rate of OH^- diffusing into the $CuFe_2O_4$ electrode is increasing with the current density, which will lead to the increase of the capacitance value. As for the current density is above 0.6 A g^{-1}, the voltage drop during the discharge course increases may play the maintainable role in determining the capacitance value with the current density increasing. As a result, specific capacitance value decreases with increasing the current density above 0.6 A g^{-1}, although the hierarchically pore structure provides high volume for electron conduction and reduces the ion diffusion paths.

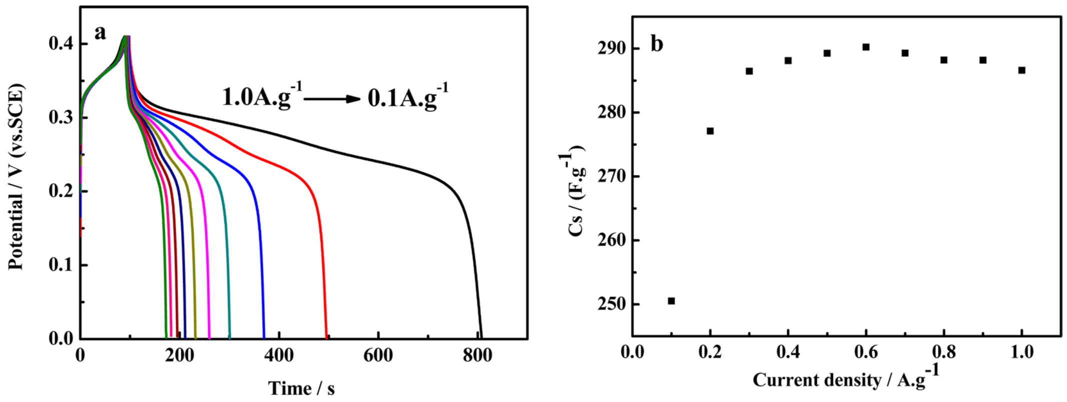

Figure 9. (a) Discharge curves of $CuFe_2O_4$ electrode at different current density and (b) the relationship between the specific capacitance and the current density.

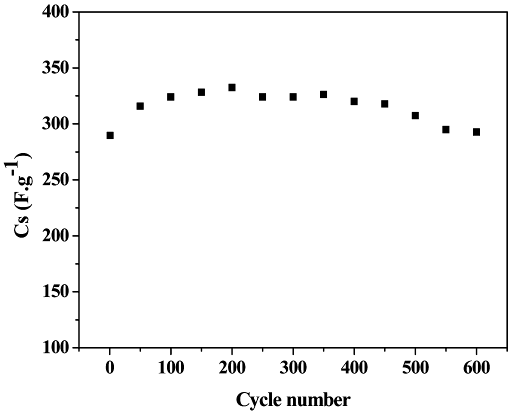

Figure 10. Specific capacitance change at a constant current of 0.6 A g^{-1} as a function of cycle number. The potential cycling was performed in 1.0 M KOH.

Figure 10 displays the variation of specific capacitance as a function of cycle number at 0.6 A g^{-1}, revealing that the hierarchically porous $CuFe_2O_4$ electrode has well recycle properties for electrochemical capacitors. It is worth noted that at the first 200 cycles there is a great increase (~15%) of capacitance and the specific capacitance reaches up to 334 F g^{-1}. Such an improvement of the specific capacitance for other materials has also been found elsewhere.[48,49] Besides the instability of cycling performance, 12% capacitance loss compared to the highest value after 600 cycles was observed. How to overcome these disadvantages will be the subject of future investigations.

Finally, we have noted that the morphology and structure of the as-prepared $CuFe_2O_4$ can be controlled by adjusting the reaction time. Also, it is well-known that the properties of nanomaterials are much dependent on their morphology as well as structure. Thus, the electrochemical properties of $CuFe_2O_4$ obtained at different reaction time were tested as a comparison, as shown in Figure 11.

As illustrated in Figure 11 A, the discharge curves for all samples indicate good capacitive behavior, and different samples show different discharge time. The specific capacitance values of all samples were shown in Figure 11B. It is noted that the $CuFe_2O_4$ nanospheres obtained at 24 h with hierarchically mesopore structure depicts the highest specific capacitance at a current of 0.6 A g^{-1}. Meanwhile, the stability of such hierarchically porous $CuFe_2O_4$ nanospheres is also satisfied.

4. CONCLUSIONS

In summary, hierarchically porous $CuFe_2O_4$ nanostructures consisting of aggregated nanocrystals have been fabricated in a solvothermal system in ethylene glycol using PVP as the structure-directing agent. Also, the possible formation mechanism of $CuFe_2O_4$ nanostructures was presented by investigating the effect of various experiment parameters. The simple, versatile, and cost-effective route reported here may provide a

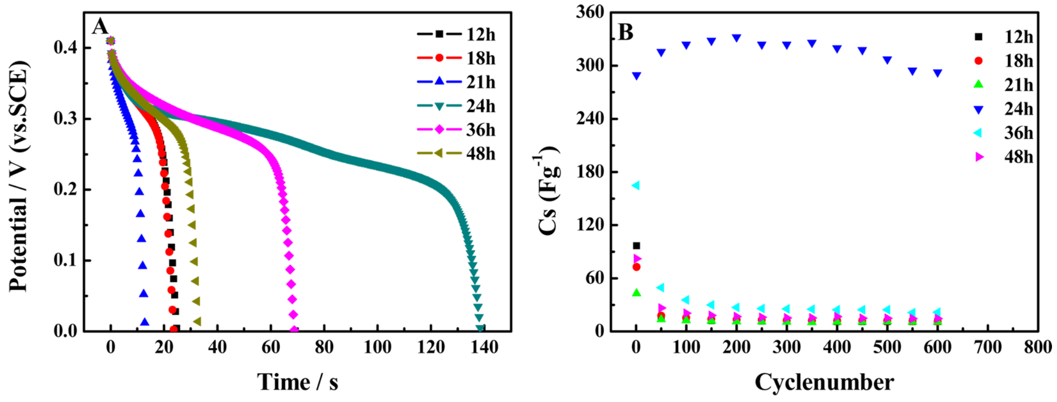

Figure 11. (A) Discharge curves and variation of specific capacitance value with cycle number at 0.6 A g^{-1} of $CuFe_2O_4$ obtained at different reaction time and (B) the specific capacitance values of all samples.

general methodology for the high-yield synthesis of metal ferrite nanostructures featuring improved properties and structures. As for application, the electrochemical measurements reveal that as-prepared $CuFe_2O_4$ with hierarchically pore structure exhibits high specific capacitance. However, the cycling performance is subject to further improvement.

■ ASSOCIATED CONTENT

Ⓢ Supporting Information

TEM images of $CuFe_2O_4$ synthesized by changing the experiment parameters, including the amount of NaAc, the type of stabilization agent, the amount of PVP as well as reaction temperature. This material is available free of charge via the Internet at http://pubs.acs.org.

■ AUTHOR INFORMATION

Corresponding Author

*E-mail: gwdiao@yzu.edu.cn.

Notes

The authors declare no competing financial interest.

■ ACKNOWLEDGMENTS

The authors gratefully acknowledge support from National Natural Science Foundation of China (Grant 21273195), a Project Funded by the Priority Academic Program Development of Jiangsu Higher Education Institutions.

■ REFERENCES

(1) Wang, G. P.; Zhang, L.; Zhang, J. J. *Chem. Soc. Rev.* **2012**, *41*, 797–828.
(2) Simon, P.; Gogotsi, Y. *Nat. Mater.* **2008**, *7*, 845–854.
(3) Miller, J. R; Simon, P. *Science* **2008**, *321*, 651–652.
(4) Su, F.; Poh, C. K.; Chen, J. S.; Xu, G.; Wang, D.; Li, Q.; Lin, J.; Lou, X. W. *Energy Environ. Sci.* **2011**, *4*, 717–724.
(5) Mai, L. Q.; Yang, F.; Zhao, Y. L.; Xu, X.; Xu, L.; Luo, Y. Z. *Nat. Commun.* **2011**, *2*, 381–385.
(6) Jiang, H.; Lee, P. S.; Li, C. *Energy Environ. Sci.* **2013**, *6*, 41–53.
(7) Winter, M.; Brodd, R. J. *Chem. Rev.* **2004**, *104*, 4245–4269.
(8) Rakhi, R. B.; Chen, W.; Cha, D. K.; Alshareef, H. N. *J. Mater. Chem.* **2011**, *21*, 16197–16204.
(9) Hu, C. C.; Chang, K. H.; Lin, M. C.; Wu, Y. T. *Nano Lett.* **2006**, *6*, 2690–2695.
(10) Liu, Y.; Zhou, F.; Ozolins, V. *J. Phys. Chem. C* **2012**, *116*, 1450–1457.
(11) Toupin, M.; Brousse, T.; Belanger, D. *Chem. Mater.* **2004**, *16*, 3184–3190.
(12) Rakhi, R. B.; Cha, D. K.; Chen, W.; Alshareef, H. N. *J. Phys. Chem. C* **2011**, *115*, 14392–14399.
(13) Meher, S. K.; Justin, P.; Ranga Rao, G. *ACS Appl. Mater. Interfaces* **2011**, *3*, 2063–2073.
(14) Meher, S. K.; Justin, P.; Ranga Rao, G. *Nanoscale* **2011**, *3*, 683–692.
(15) Lang, J. W.; Kong, L. B.; Wu, W. J.; Luo, Y. C.; Kang, L. *Chem. Commun.* **2008**, 4213–4215.
(16) Pang, H.; Gao, F.; Chen, Q.; Liu, R.; Lu, Q. *Dalton Trans.* **2012**, *41*, 5862–5868.
(17) Rakhi, R. B.; Chen, W.; Cha, D.; Alshareef, H. N. *Nano Lett.* **2012**, *12*, 2559–2567.
(18) Wang, X.; Sumboja, A.; Khoo, E.; Yan, C.; Lee, P. S. *J. Phys. Chem. C* **2012**, *116*, 4930–4935.
(19) Xia, X. H.; Tu, J. P.; Mai, Y. J.; Wang, X. L.; Gu, C. D.; Zhao, X. B. *J. Mater. Chem.* **2011**, *21*, 9319–9325.
(20) Meher, S. K.; Ranga Rao, G. *J. Phys. Chem. C* **2011**, *115*, 25543–25556.
(21) Cheng, Y.; Zou, B.; Wang, C.; Liu, Y.; Fan, X.; Zhu, L.; Wang, Y.; Ma, H.; Cao, X. *CrystEngComm* **2011**, *13*, 2863–2870.
(22) Zhu, M.; Wang, Y.; Meng, D.; Qin, X.; Diao, G. *J. Phys. Chem. C* **2012**, *116*, 16276–16285.
(23) Brezesinski, T.; Wang, J.; Tolbert, S. H.; Dunn, B. *Nat. Mater.* **2010**, *9*, 146–151.
(24) Wee, G.; Soh, H. Z.; Yan, C. L.; Mhaisalkar, S. G.; Srinivasan, M. *J. Mater. Chem.* **2010**, *20*, 6720–6725.
(25) Zhu, J.; Shi, W.; Xiao, N.; Rui, X.; Tan, H.; Lu, X.; Hng, H. H.; Ma, J.; Yan, Q. *ACS Appl. Mater. Interfaces* **2012**, *4*, 2769–2774.
(26) Qiu, G.; Huang, H.; Dharmarathna, S.; Benbow, E.; Stafford, L.; Suib, S. L. *Chem. Mater.* **2011**, *23*, 3892–3901.
(27) Wu, C. H.; Ma, J. S.; Lu, C. H. *Current Appl. Phys.* **2012**, *12*, 1058–1063.
(28) Yan, W. B.; Ayvazian, T.; Kim, J. Y.; Liu, Y.; Donavan, K. C.; Xing, W. D.; Yang, Y. A.; Hemminger, J. C.; Penner, R. M. *ACS Nano* **2011**, *5*, 8275–8287.
(29) Chen, S.; Zhu, J. W.; Wu, X. D.; Han, Q. F.; Wang, X. *ACS Nano* **2010**, *4*, 2822–2830.
(30) Wu, Z. S.; Ren, W. C.; Wang, D. W.; Li, F.; Liu, B.; Cheng, H. M. *ACS Nano* **2010**, *4*, 5835–5842.
(31) Qiu, G.; Dharmarathna, S.; Zhang, Y.; Opembe, N.; Huang, H.; Suib, S. L. *J. Phys. Chem. C* **2012**, *116*, 468–477.
(32) Zhang, X.; Shi, W.; Zhu, J.; Kharistal, D. J.; Zhao, W.; Lalia, B. S.; Hng, H. H.; Yan, Q. *ACS Nano* **2011**, *5*, 2013–2019.
(33) Zhang, M.; Guo, S.; Zheng, L.; Zhang, G.; Hao, Z.; Kang, L.; Liu, Z. H. *Electrochim. Acta* **2013**, *87*, 546–553.
(34) Lu, Q.; Chen, Y.; Li, W.; Chen, J. G.; Xiao, J. H.; Jiao, F. *J. Mater. Chem. A* **2013**, *1*, 2331–2336.
(35) Ren, Y.; Ma, Z.; Bruce, P. G. *CrystEngComm* **2011**, *13*, 6955–6959.
(36) Pang, H.; Deng, J.; Wang, S.; Li, S.; Du, J.; Chen, J.; Zhang, J. *RSC Adv.* **2012**, *2*, 5930–5934.
(37) Kuo, S. L.; Wu, N. L. *Electrochem. Solid-State Lett.* **2007**, *10*, A171–A175.
(38) Wang, Q.; Wang, X.; Liu, B.; Yu, G.; Hou, X.; Chen, D.; Shen, G. *J. Mater. Chem. A* **2013**, *1*, 2468–2473.
(39) Zhang, G.; Wu, H. B.; Hoster, H. E.; Chan-Park, M. B.; Lou, X. W. *Energy Environ. Sci.* **2012**, *5*, 9453–9456.
(40) Zhao, J.; Cheng, Y.; Yan, X.; Sun, D.; Zhu, F.; Xue, Q. *CrystEngComm.* **2012**, *14*, 5879–5885.
(41) Fu, Y.; Chen, Q.; He, M.; Wan, Y.; Sun, X.; Xia, H.; Wang, X. *Ind. Eng. Chem. Res.* **2012**, *51*, 11700–11709.
(42) Nedkov, I.; Vandenberghe, R. E.; Marinova, T.; Thailhades, Ph.; Merodiiska, T.; Avramova, I. *Appl. Surf. Sci.* **2006**, *253*, 2589–2596.
(43) Wu, Y.; He, Y.; Wu, T.; Chen, T.; Weng, W.; Wan, H. *Mater. Lett.* **2007**, *61*, 3174–3178.
(44) Banfield, J. F.; Welch, S. A.; Zhang, H.; Ebert, T. T.; Penn, R. L. *Science* **2000**, *289*, 751–754.
(45) Alivisatos, A. P. *Science* **2000**, *289*, 736–737.
(46) Reddy, R. N.; Reddy, R. G. *J. Power Sources* **2004**, *132*, 315–320.
(47) Ham, D.; Chang, J. H.; Pathan, S. H.; Kim, W. Y.; Mane, R. S.; Pawar, B. N.; Joo, O. S.; Chung, H.; Yoon, M. Y.; Han, S. H. *Curr. Appl. Phys.* **2009**, *9*, S98–S100.
(48) Toupin, M.; Brousse, T.; Bélanger, D. *Chem. Mater.* **2002**, *14*, 3946–3952.
(49) Pang, S. C.; Anderson, M. A.; Chapman, T. W. *J. Electrochem. Soc.* **2000**, *147*, 444–450.